CRYSTAL GROWTH & DESIGN

Article

Cite This: Cryst. Growth Des. 2019, 19, 2279−2288

pubs.acs.org/crystal

Understanding the Hydration Process of Salts: The Impact of a Nucleation Barrier

Leyla-Cann Sögütoglu,[†] Michael Steiger,[‡] Jelle Houben,[†] Daan Biemans,[†] Hartmut R. Fischer,[¶] Pim Donkers,[¶] Henk Huinink,*[,†] and Olaf C. G. Adan[†,¶]

[†]Department of Applied Physics, Technical University Eindhoven, Den Dolech 2, 5600 MB Eindhoven, The Netherlands

[‡]Department of Chemistry, University of Hamburg, Martin-Luther-King-Platz 6, 20146 Hamburg, Germany

[¶]TNO, High Tech Campus 25, 5656 AE Eindhoven, The Netherlands

Supporting Information

ABSTRACT: The solid-state hydration of salts has gained particular interest within the frame of thermochemical energy storage. In this work, the water vapor pressure−temperature ($p-T$) phase diagram of the following thermochemical salts was constructed by combining equilibrium and nonequilibrium hydration experiments: $CuCl_2$, K_2CO_3, $MgCl_2{\cdot}4H_2O$, and LiCl. The hydration of $CuCl_2$ and K_2CO_3 involves a metastable zone of ca. 10 K, and the induction times preceding hydration are well-described by classical homogeneous nucleation theory. It is further shown for K_2CO_3 (metastable) and $MgCl_2{\cdot}4H_2O$ (not metastable) through solubility calculations that the phase transition is not mediated by bulk dissolution. We conclude that the hydration proceeds as a solid−solid phase transition, mobilized by a wetting layer, where the mobility of the wetting layer increases with increasing vapor pressure. In view of heat storage application, the finding of metastability in thermochemical salts reveals the impact of nucleation and growth processes on the thermochemical performance and demonstrates that practical aspects like the output temperature of a thermochemical salt are defined by its metastable zone width (MZW) rather than its equilibrium phase diagram. Manipulation of the MZW by e.g. prenucleation or heterogeneous nucleation is a potential way to raise the output temperature and power on material level in thermochemical applications.

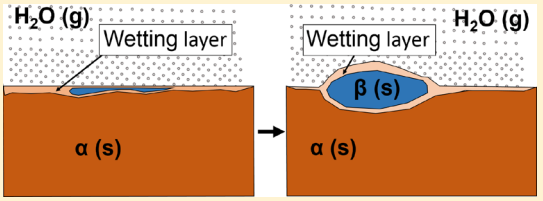

INTRODUCTION

Hydration of salts has gained large interest in the past decade for the purpose of thermochemical heat storage.[1−4] In general, heat storage is an essential aid for most of the renewable, fluctuating energy sources. The specific concept of thermochemical heat storage emerged in the 1960s,[5] and although research and development in this area remained at an early stage for a long time, multidisciplinary studies have been revived recently, focusing on practical aspects like the charging/discharging temperature and volumetric storage density of the thermochemical material.[6−11]

A salt acts as a thermochemical material by the following hydration reaction:

$$MX{\cdot}aH_2O(s) + (b-a)H_2O(g) \rightleftharpoons MX{\cdot}bH_2O(s) \qquad (I)$$

The heat is stored in the solid material $MX{\cdot}aH_2O$ (phase α), when gaseous water is desorbed and is released in the form of binding enthalpy, when the gaseous water reabsorbs to form solid material $MX{\cdot}bH_2O$ (phase β). In this way, the salt functions as a heat battery.

The hydration of a salt is a complex process where mass and heat transfer accompany the exothermic binding of water, with typical volume expansions of 50% due to drastic changes in the crystal structure. With this complex interplay in mind, a thermochemical salt can be described in a simplified way as a structure α decomposing and reorganizing into structure β upon absorption of gaseous water. The latter is known as a structural phase transition.

Structural phase transitions and mechanisms have been studied extensively for dehydration.[12,13] However, mechanisms of hydration are less pronounced; these studies require a well-defined relative humidity (RH) and temperature, which can be an experimental challenge. The hydration of pharmaceutically active compounds is reported usually at ambient conditions, focusing on the stability of the pharmaceutical[14,15] and hydration studies of thermochemical salts as a function of RH are relatively scarce.[16−19]

Based on the present literature, two main pathways can be hypothesized for the hydration of a crystalline salt: (I) a direct solid−solid transition, reported for symmetry related (topotactic) start and end structures[20] and (II) a two-step pathway, where liquid formation mediates the solid-state transition.[16] The two pathways are schematically depicted in Figure 1.

This work aims to shed light on the hydration process of crystalline salts within the frame of thermochemical heat storage. To this end, four salts (reactions i−iv) were studied,

Received: December 24, 2018
Revised: February 8, 2019
Published: February 14, 2019

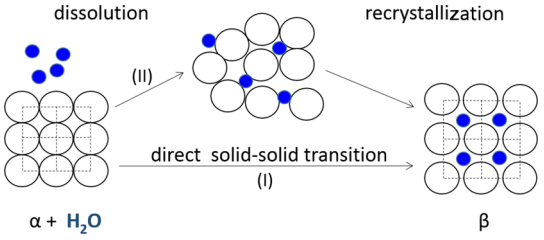

Figure 1. Two possible pathways of hydration: (I) a direct solid–solid transition and (II) a solution-mediated transition. α and β represent different crystal structures; water molecules are represented by the smaller filled circles.

listed among the most suitable systems for heat storage in domestic application.[8]

$$CuCl_2(s) + 2H_2O(g) \rightleftharpoons CuCl_2{\cdot}2H_2O(s) \quad (i)$$

$$K_2CO_3(s) + 1.5H_2O(g) \rightleftharpoons K_2CO_3{\cdot}1.5H_2O(s) \quad (ii)$$

$$MgCl_2{\cdot}4H_2O(s) + 2H_2O(g) \rightleftharpoons MgCl_2{\cdot}6H_2O(s) \quad (iii)$$

$$LiCl(s) + H_2O(g) \rightleftharpoons LiCl{\cdot}H_2O(s) \quad (iv)$$

In this study, it is demonstrated that reactions i and ii proceed as a solid-to-solid phase transition according to classical homogeneous nucleation with a metastable zone width of ca. 10 K. In the same experimental conditions, reactions iii and iv occur nearly instantaneous at equilibrium. The difference in hydration behavior is considered in view of recent literature on the dissolution of the metastable phase. Finally, the thermochemical performance of the investigated salts is presented in view of the present insights.

THEORETICAL BACKGROUND

Although it is impossible to truly detect the moment of nucleation and the actual nucleation rate, the inverse of the observable induction period is often taken as a measure of the latter.[21] In this section we briefly summarize the key aspects of nucleation theory applied to hydration.[22] For details, the reader is referred to Supporting Information S1.

The induction period τ [s] is defined as the period of time which elapses between the achievement of supersaturation and the start of rapid desupersaturation[23] and is given by

$$\tau \equiv \frac{c}{J} \quad (1)$$

where J [s^{-1}] is the actual nucleation rate and c [−] is a proportionality constant. The induction period has a stochastic nature[24] and may be considered as a sum of several parts:

$$\tau = t_r + t_n + t_g + t_{lp} \quad (2)$$

with t_r [s] a "relaxation time" to reach a quasi steady-state distribution of molecular clusters; t_n [s] a time required to form a stable nucleus (i.e., a cluster of critical size), and t_g [s] a time for the nucleus to grow to a detectable size. Often a latent period t_{lp} [s] follows t_g [s], during which no noticeable change in size is observed, until an accelerated growth period starts, dominated by crystal growth only.[23]

The nucleation rate J can be expressed in the form of an Arrhenius-like reaction rate equation, containing a kinetic parameter κ [s^{-1}] (not further parametrized here) and the classical energy barrier ΔG^* [J]:

$$J = \kappa \exp\left(\frac{-\Delta G^*}{k_B T}\right) \quad (3)$$

where k_B is the Boltzmann constant [1.38×10^{-23} J/K] and T [K] is the absolute temperature.

It is not straightforward to predict the shape and location of the nucleus. Hydration might involve the formation of the hydrate salt cluster on or partially in the dehydrated crystal. Two main scenarios are possible: (1) The β cluster grows layer-by-layer on the surface of the α phase. This is the case for a deposition type of growth. That is, the interfacial energy between phase β and its surrounding acts only at the radial direction of the cluster, causing 2D layer-by-layer growth. (2) The β cluster grows in an overlayer mode. This is the case for a nucleation point which expands uniformly. That is, the interfacial energy between β and surrounding acts uniformly from all orientations, causing a 3D growth.[23,25] The considered nucleus shapes are schematically represented in Figure 2.

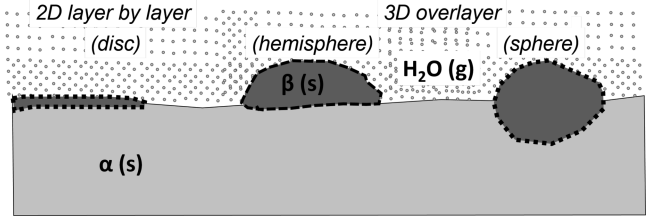

Figure 2. Schematic cartoon (side view) of nucleus shapes. The hydrated phase β nucleates by absorption of gaseous water from the atmosphere. In the case of a 2-dimensional nucleus, growth proceeds layer by layer. In case of a 3D nucleus, growth proceeds as an expanding sphere. The nucleus has an interface (dotted line) with its surrounding.

It should be noted that partial dissolution of the surface layer of the crystal is possible. Further hydration of the crystal would in this case involve transport of water to the inner parts of the crystal via e.g. the interface between nucleus and crystal (dotted line in Figure 2). Especially the 3D scenario may involve partial dissolution, since there is migration of the solid.

For a 2D and 3D scenario, the critical cluster size r^* and the corresponding energy barrier for nucleation ΔG^* are

$$r^*_{2D} = \frac{v\gamma}{(b-a)k_B T \ln p/p_{eq}} \quad (4)$$

$$r^*_{3D} = \frac{2v\gamma}{(b-a)k_B T \ln p/p_{eq}} \quad (5)$$

and

$$\Delta G^*_{2D} = \frac{h\pi v\gamma^2}{(b-a)k_B T \ln(p/p_{eq})} \quad (6)$$

$$\Delta G^*_{3D} = \frac{\eta\pi v^2\gamma^3}{(b-a)^2(k_B T)^2 \ln^2(p/p_{eq})} \quad (7)$$

where h [m] is the height of a disclike 2D cluster, typically angstrom-scale corresponding to a monolayer of growth units, v [m^3] is the volume of one hydrated salt unit $MX{\cdot}bH_2O$, γ [J/m^2] is the interfacial surface energy, and p/p_{eq} [−] is the supersaturation in terms of the partial water vapor pressure p [mbar] and the equilibrium vapor pressure p_{eq} [mbar].

DOI: 10.1021/acs.cgd.8b01908
Cryst. Growth Des. 2019, 19, 2279−2288

Further, b [−] is the number of water molecules per salt unit in phase β and a [−] is the number of water molecules per salt unit in phase α. Finally, η [−] is a shape factor for the 3D cluster, which is 16/3 for a sphere and 8/3 for half a sphere (hemisphere). The material parameters a, b, v, and h are listed for $CuCl_2$ and K_2CO_3 in Table 1. For details on the derivation of the equations we refer to Supporting Information S1.

Table 1. Nucleation Rate Parameters for $CuCl_2 \cdot 2H_2O$ and $K_2CO_3 \cdot 1.5H_2O$[a]

	$CuCl_2$	K_2CO_3
a	0	0
b	2	1.5
v (m^3)	112.3×10^{-30}	124.0×10^{-30}
h (m)	7.414×10^{-10}	7.1093×10^{-10}

[a]The height h is taken here as the unit cell axis which is parallel to the layer of water molecules in the hydrated structure.[26,27]

MATERIALS AND METHODS

Sample Preparation. $K_2CO_3 \cdot 1.5H_2O$ (pro analysis) was purchased from Sigma-Aldrich, and $CuCl_2 \cdot 2H_2O$, $MgCl_2 \cdot 6H_2O$, and LiCl (pro analysis) were purchased from Merck. Salts were sieved to 50−164 μ m size fraction and used without any further purification. K_2CO_3 was preheated to 120 °C to purify the compound from any possible bicarbonate impurity.[28]

Pressure−Temperature Measurements (p,T-meter). The experimental setup to measure equilibrium phase lines is shown schematically in Figure 3. The pressure−temperature (p−T) setup

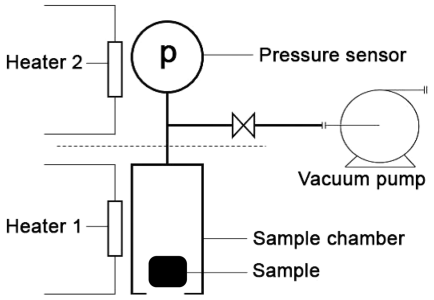

Figure 3. Schematic representation of the pressure−temperature measurement setup, used to measure equilibrium phase lines of salt hydrates. The system is thermally isolated. Sample and surrounding are brought to the same temperature simultaneously using heater 1 and 2, respectively. After equilibration, the water vapor pressure is measured using a pressure sensor.

consists of a stainless steel sample chamber which is connected to an Arduino absolute pressure sensor via a valve to a vacuum pump. Tubing consists of 6 mm outside diameter stainless steel and connections are made with Swagelok fittings. The sample chamber which needs frequent assembly and disassembly is connected via a KF flange with a rubber O-ring, which is mated by a circumferential clamp. The sample chamber is heated with an electric band heater and the temperature is controlled with an Eurotherm 2216e controller. The complete setup is heated with an electric heating wire and all parts are insulated to avoid internal condensation. For measuring the equilibrium phase line, approximately 1 g of the hydrated salt is positioned inside the sample chamber. After evacuating the sample chamber, the chamber is heated and the temperature is kept constant until an equilibrium pressure is reached. It is assumed that the amount of water during dehydration to arrive at an equilibrium pressure is negligible compared with the amount present in the hydrated salt. The temperature is increased stepwise, and the next equilibrium pressure is determined. From these data points the equilibrium vapor pressure line is constructed as a function of temperature.

Thermogravimetric Analysis (TGA). A thermogravimetric analyzer of type Mettler-Toledo TGA/SDTA 851e was equipped with a home-built humidity generator (Figure 4). The purge gas (air

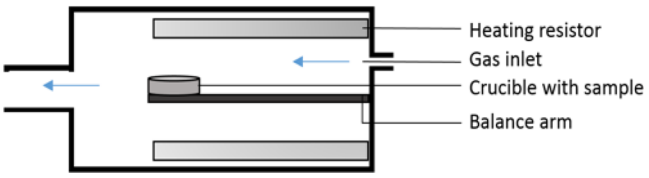

Figure 4. Schematic representation of the thermogravimetric analyzer, used to measure hydration (and dehydration) onset points of salts. The sample is placed inside the oven, and the oven is cooled (and heated) with typical rates of 0.1−5 K/min while the oven is purged with air with fixed water vapor pressure.

flow with a rate of 500 mL/min) was brought to the desired water vapor pressure by mixing dry gas (air with 0% RH) and wet gas (100% RH) at a controlled temperature of 21 °C. The water vapor pressure was calibrated with an accuracy of ±0.5 mbar using the gravimetric signal at the deliquescence point of $LiCl \cdot H_2O$, CH_3COOK, $K_2CO_3 \cdot 1.5H_2O$, $MgCl_2 \cdot 6H_2O$, and $MgNO_3 \cdot 6H_2O$ at 25 °C and $LiCl \cdot H_2O$ at 40, 50, 55, and 60 °C.[29] Temperature calibration was performed using the simultaneous differential thermal analysis (SDTA) signal of melting points of indium, zinc, and aluminum. In the case of an endothermic process such as melting, a differential signal is observed.[30] Approximately 5 mg of the hydrated salt was placed in a 40 μ L Mettler-Toledo standard aluminum pan without a lid, and samples were dehydrated and rehydrated at fixed water vapor pressure p at various heating/cooling rates: 0.1, 0.2, 0.5, 1, 2, and 5 K/min. Actual sample temperatures were recorded at the bottom of the pan and the relative humidity was recorded at the outlet of the TGA oven using a Sensirion capacitive humidity sensor.

RESULTS AND DISCUSSION

Metastable Zone. The phase diagram of salt hydrates (Figure 5) was mapped by plotting the partial water vapor pressure p of the salt against the temperature T of the salt. The thermodynamically distinct phases were identified based on the sample mass and validated using powder XRD.

Equilibrium (p,T) values were obtained using the p,T-meter, by measuring absolute vapor pressures at steady sample temperature (Figure 6a). The experimental values match the equilibrium pressures in literature to a satisfactory extent.[31−34] Metastable zone width (MZW) values were measured using TGA, by heating/cooling the salt at a fixed vapor pressure and detecting the onset temperature at various heating/cooling rates (Figure 6b).

Based on Figure 5, a clear difference between the equilibrium pressure and the thermogravimetric onset pressure (called the critical pressure p^* hereafter) for hydration and dehydration are observed for $CuCl_2$ (a) and K_2CO_3 (b). An in-depth study on the dehydration of $CuCl_2$ appeared recently.[13] The rest of the paper focuses on the hydration behavior only.

For $CuCl_2$ and K_2CO_3, the critical pressure for hydration is significantly higher than the equilibrium phase line. $MgCl_2$ (c) and LiCl (d) on the other hand have a much smaller to virtually no difference between the equilibrium pressure and the critical pressure. Among the investigated compounds, K_2CO_3 hydration was reported earlier (1984) as kinetically hindered, without further experimental elaboration on the low vapor pressure region.[19]

DOI: 10.1021/acs.cgd.8b01908
Cryst. Growth Des. 2019, 19, 2279−2288

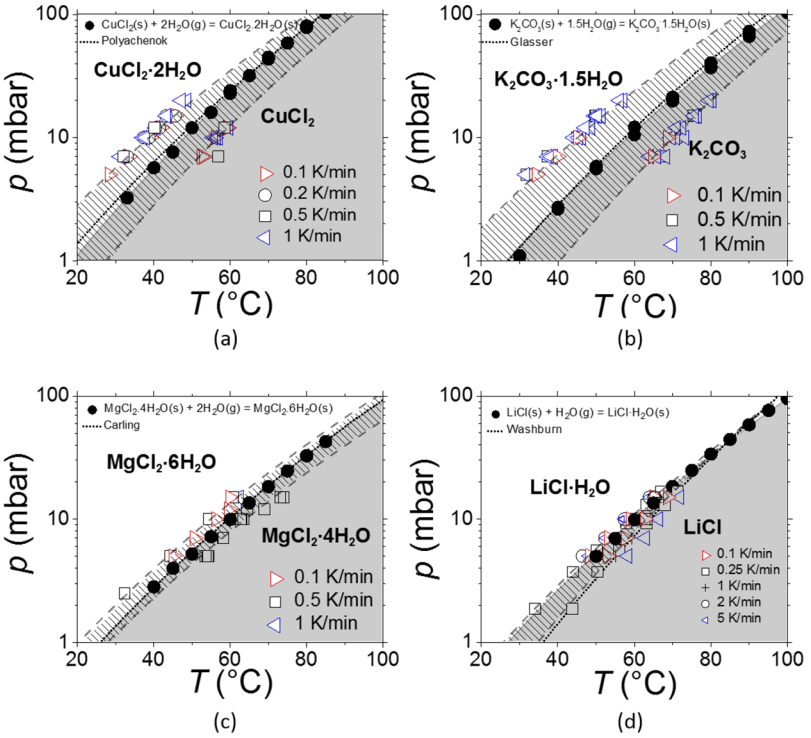

Figure 5. Experimental phase diagrams of (a) $CuCl_2$, (b) K_2CO_3, (c) $MgCl_2{\cdot}4H_2O$, and (d) LiCl. p is the partial water vapor pressure. Solid symbols represent equilibrium pressures at steady sample temperature. Open symbols represent the onset temperatures for hydration at fixed vapor pressure. Equilibrium pressures and critical pressures were plotted with the Clausius–Clapeyron relation as a guide to the eye, displayed by the solid and dashed lines, respectively. Equilibrium pressures from the literature are indicated by the dotted lines.[31−34] The inactive (metastable) zone is hatched.

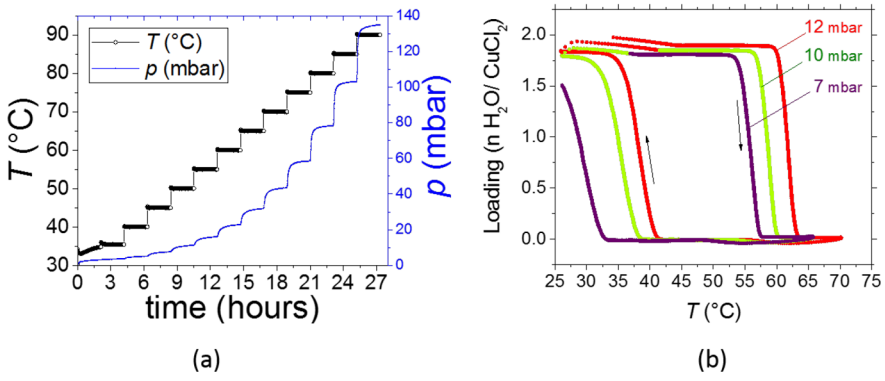

Figure 6. Example of an equilibrium (a) and kinetic (b) measurement for construction of pressure–temperature phase diagrams: (a) equilibrium pressures of $CuCl_2{\cdot}2H_2O$, equilibration time 2 h; (b) heating and cooling of $CuCl_2{\cdot}2H_2O$ at water vapor pressure p = 7, 10, and 12 mbar. Heating/cooling rate 0.1 K/min.

Nucleation and Growth. After mapping the equilibrium phase line and the critical pressure p^*, hydration experiments were performed on $CuCl_2$ and K_2CO_3 at supersaturations below p^*.

Conversion below p^* proceeds only after an induction period, illustrated for $CuCl_2$ in Figure 7. When a supersaturation (Figure 7a) is applied at point A in time (Figure 7b), an induction period τ passes until accelerated water uptake begins at point B. Point B denotes the extrapolated onset point of the hydration and was taken as the induction period τ.[35]

A second observation below p^* is the following: if the induction period at a supersaturation (I) is not completed (Figure 8), but the salt is allowed to induce at a higher supersaturation (II), conversion proceeds instantaneously when the pressure is readapted to supersaturation (I) where initially no reaction was observed. The absence of induction after the partial conversion points toward a nucleation barrier below the critical pressure. Other possible rate-limiting processes, like e.g. diffusion or surface reorganization, do not explain the observation in Figure 8.

The critical pressure found in isobaric cooling experiments (dashed line in Figure 9a, c) was compared with isothermal induction time experiments as a function of the supersaturation (Figure 9b, d). The induction time increases exponentially close to equilibrium and is on the order of minutes at the metastable zone boundary. The present findings support the

DOI: 10.1021/acs.cgd.8b01908
Cryst. Growth Des. 2019, 19, 2279−2288

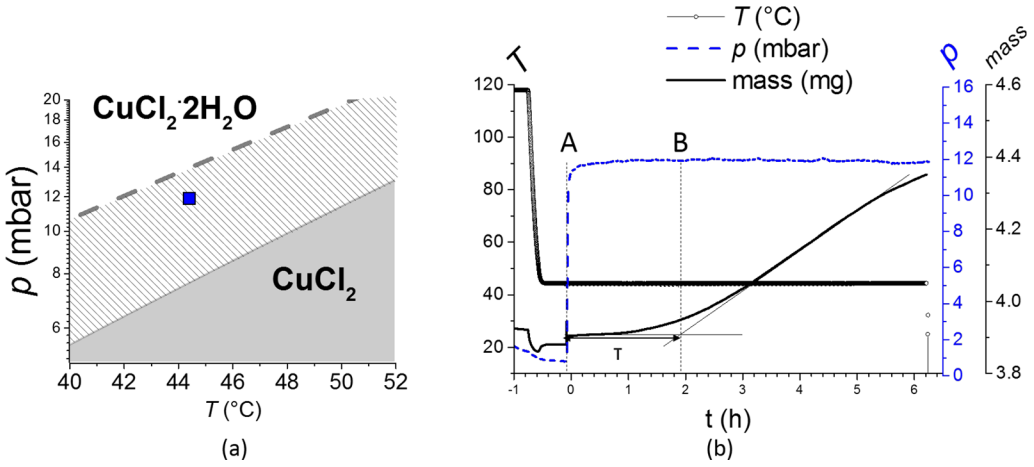

Figure 7. (a) Phase diagram indicating T = 44 °C and p = 12 mbar. (b) Thermogram of $CuCl_2$ at the conditions in part a. Supersaturation is created at point A by applying p = 12 mbar at 44 °C after 20 min of dehydration using dry air (p = 0 mbar) at 120 °C.

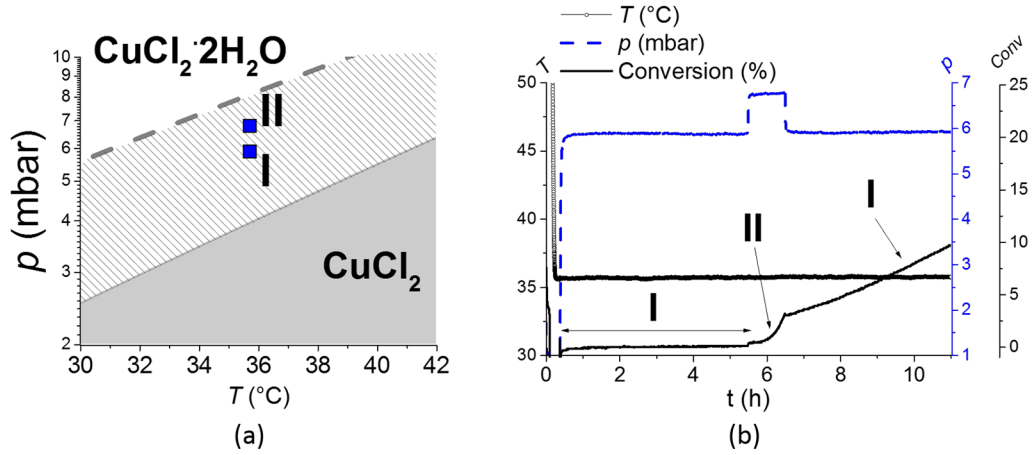

Figure 8. (a) Phase diagram indicating T = 36 °C and p = 6 and 6.8 mbar. (b) Thermogram of $CuCl_2$ showing the hydration progress at the conditions in part a.

idea of a nucleation event during the induction period, where p^* is the metastable zone boundary.

Nucleation. Based on the surface to volume consideration of a cluster of a hydrated salt unit, the induction time τ is expected to have the following relation with respect to the supersaturation p/p_{eq}:

$$\ln(\tau^{-1}) = \ln\left(\frac{\kappa}{c}\right) - \lambda\frac{1}{[\ln(p/p_{eq})]^n} \quad (8)$$

with n = 1 and 2 for 2D and 3D nucleation respectively, κ [s^{-1}] the so-called kinetic parameter (not further elaborated), c[−] is a constant, and λ [−] is the thermodynamic parameter, which contains the interfacial surface energy γ and relates to the energy barrier for nucleation:

$$\lambda_{2D} = \frac{h\pi v\gamma^2}{(kT)^2(b-a)} \quad (9)$$

and

$$\lambda_{3D} = \frac{\eta\pi v^2\gamma^3}{(kT)^3(b-a)^2} \quad (10)$$

Figure 10 shows the linear fit according to eq 8 for hydration experiments of $CuCl_2$ and K_2CO_3. The experimental fit is in accordance with both a 2D and 3D nucleation model. Figure 11 shows the interfacial energy as a function of temperature, assumed to be isotropic and determined using the slopes in Figure 10.

The γ-value is in both hydration experiments 10−15 mJ/m^2 when a spherical (3D) geometry is assumed and amounts 20−25 mJ/m^2 in the assumption of a disc (2D) geometry. Comparable γ-values were found for the interfacial energies of salt/solution interfaces, e.g. Na_2CO_3, KI, and Ni-$(NH_4)_2(SO_4)_2{\cdot}6H_2O$.[21,36,37] A decrease of the interfacial energy with increasing temperature is expected based on the literature,[36] and $CuCl_2$ shows an anomaly in this respect at 44 °C. It is noteworthy that the γ-values in this study are significantly lower than typical interfacial energies of liquid−gas or solid−gas interfaces.[38]

Finally, the critically sized cluster was evaluated as a function of supersaturation, shown in Figure 12. At the critical pressure (i.e., the metastable zone boundary), the critically sized cluster is one to several salt units and the corresponding free energy of nucleation is ΔG^* is 5−20 kJ/mol. It should be noted that the critical cluster size based on the induction time is a thermodynamic quantity and does not reveal any detail about, e.g., the reversibility of the surface absorption or the chemical reaction in the bulk.

DOI: 10.1021/acs.cgd.8b01908
Cryst. Growth Des. 2019, 19, 2279−2288

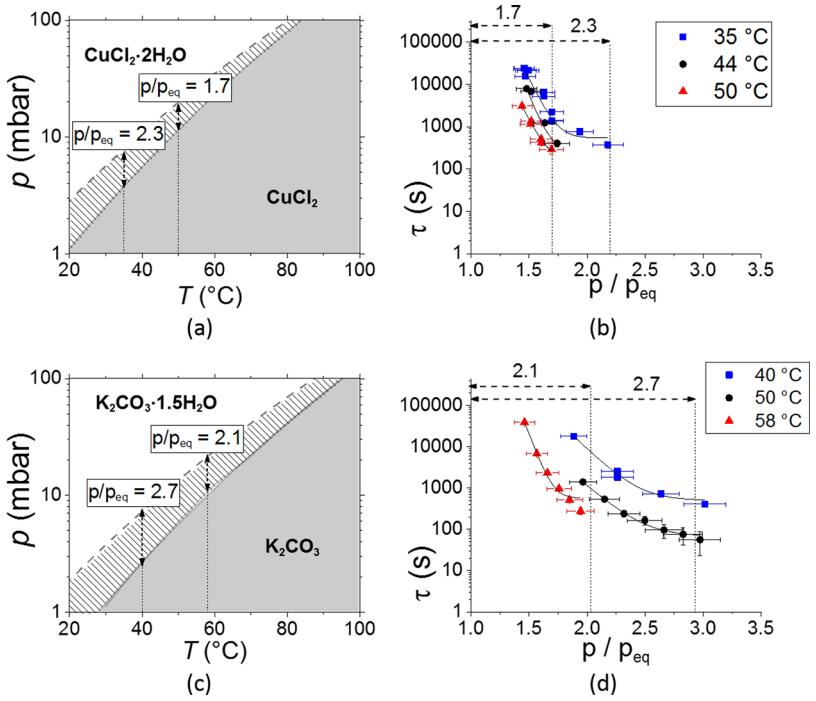

Figure 9. (a, c) Phase diagrams of $CuCl_2$ and K_2CO_3 showing the metastable zone based on isobaric cooling experiments in TGA. The metastable zone is hatched. (b, d) Induction times of $CuCl_2$ and K_2CO_3 respectively plotted against the driving force p/p_{eq} in isothermal experiments.

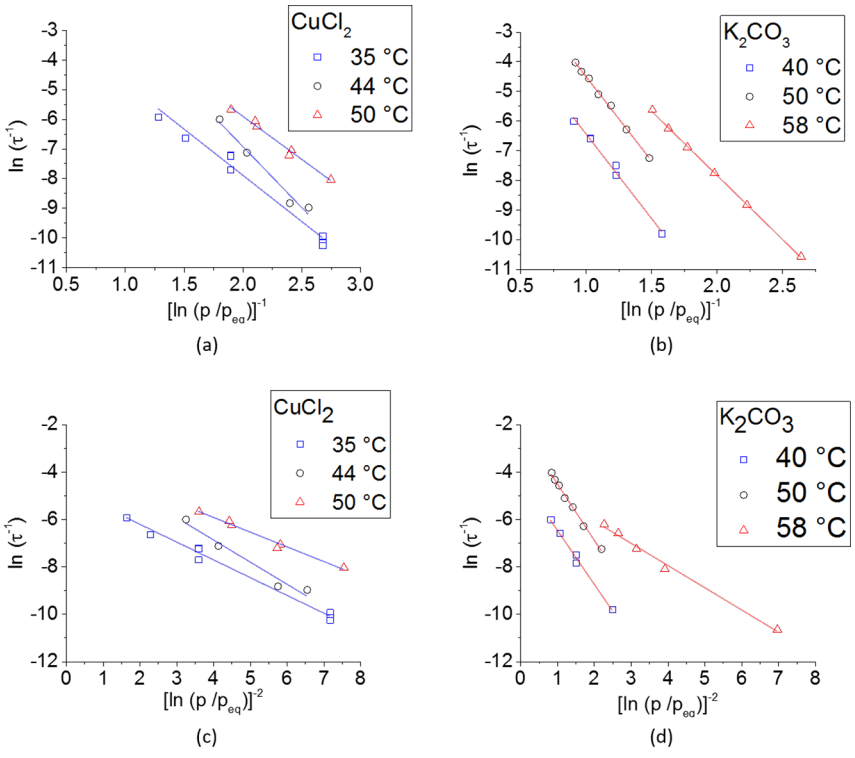

Figure 10. Dependence of the induction time on the supersaturation degree. Linear fit according to 2D nucleation (top) and 3D nucleation (bottom). Samples and temperatures are indicated in the legends.

At supersaturations >3, the nucleus size decreases at some temperatures below one water−salt unit, which cannot be interpreted on the basis of the classical nucleus formation. The corresponding nucleation barrier ΔG^* is ca. 2.7 kJ/mol (which is the thermal energy at 50 °C). In other words, the available thermal energy at this supersaturation is sufficient for a continuous conversion irrespective of the nucleus.

Growth. To investigate the relation between nucleation and growth, isothermal conversion rates at 40 °C for K_2CO_3 were plotted as a function of the supersaturation (Figure 13a, b). The conversion rate was also plotted as a function of the inverse of the preceding induction time (13c).

The rate of conversion increases monotonically with the supersaturation: the near-equilibrium hydration rate starts low

DOI: 10.1021/acs.cgd.8b01908
Cryst. Growth Des. 2019, 19, 2279−2288

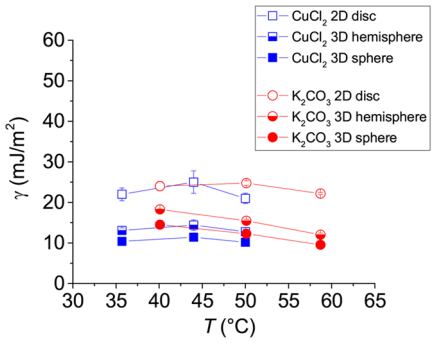

Figure 11. Interfacial energies γ obtained after fitting the induction time against supersaturation according to a 2D disc and 3D hemisphere nucleation model: $CuCl_2$ (squares) and K_2CO_3 (circles).

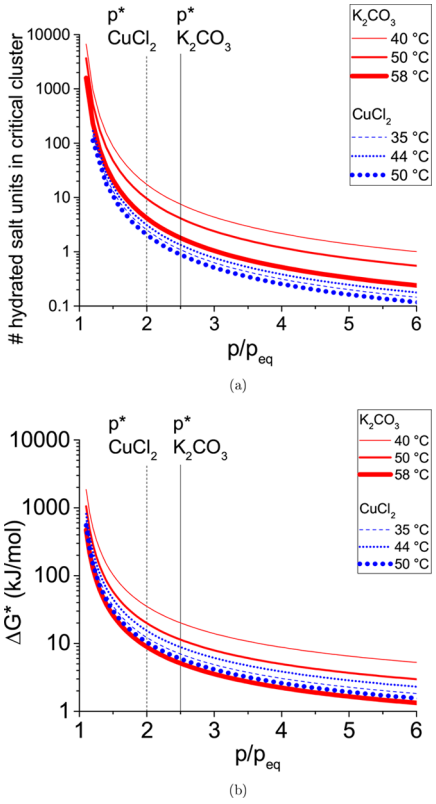

Figure 12. (a) Nucleus size as a function of supersaturation for K_2CO_3 (solid lines) and $CuCl_2$ (dashed lines). The average critical pressure is indicated by the vertical lines. (b) The Gibbs free energy for nucleation as a function of supersaturation. A nucleus size below one water−salt unit cannot be interpreted on the basis of the classical nucleus formation and is rather a stage with continuous conversion, irrespective of the nucleus size.

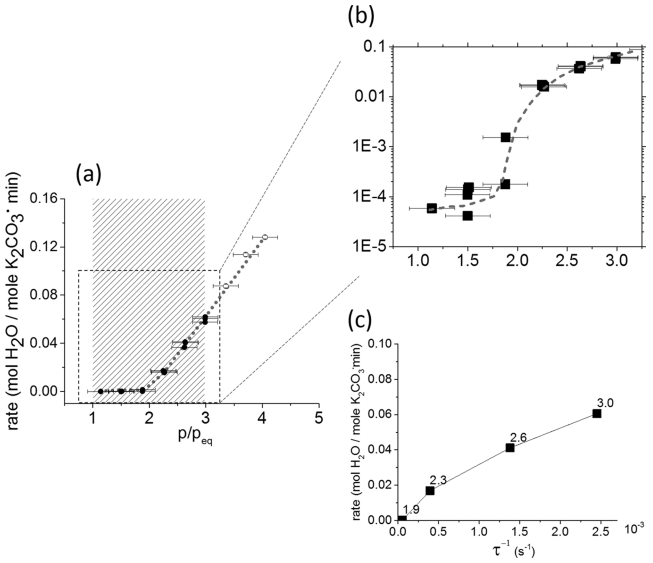

Figure 13. (a) Rate of hydration as a function of supersaturation p/p_{eq} for K_2CO_3. Measurements with noticeable induction times are shown by solid symbols; measurements with instantaneous conversion (i.e., no significant induction time) are shown by open symbols. The metastable zone is hatched. (b) Log-scale plot of the boxed region. (c) Conversion rate plotted against the induction time. The corresponding supersaturations are indicated as labels.

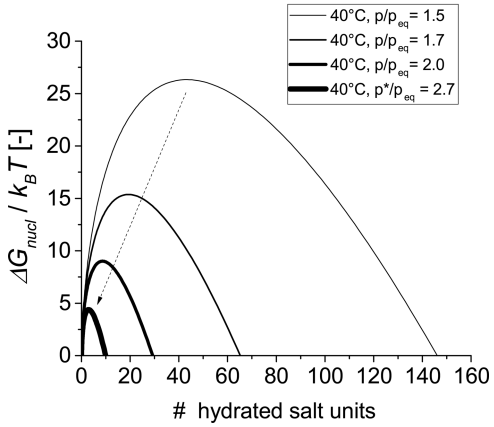

Figure 14. Change of Gibbs free energy for nucleation at different supersaturations as a function of the cluster size.

at 10^{-4} mol H_2O/mol K_2CO_3·min and increases rapidly at the metastable zone boundary to 10^{-2} mol H_2O/mol K_2CO_3·min (Figure 13b). Figure 13c shows that below the metastable zone boundary, the conversion is proportional to the nucleation rate: nucleation seems to limit the overall conversion in the metastable region.

Figure 14 shows the change in Gibbs free energy as a function of cluster size at different supersaturations, scaled with respect to the thermal energy k_BT. As expected from the limited conversion rate, the nucleation barrier in the metastable zone is significantly higher than the available thermal energy and reaches the order of the thermal energy at the critical supersaturation $p^*/p_{eq} \sim 2.7$. Above p^*, the conversion rate is linear with the supersaturation with typical values of 10^{-1} mol H_2O/mol K_2CO_3·min.

Dissolution of the Metastable Phase. In this section, the present results on nucleation and growth are viewed in light of literature. In a recent study by Steiger et al., it was reported for the hydration of $MgSO_4·H_2O$ (phase α) to $MgSO_4·6H_2O$ (phase β) that the mechanism and kinetics of hydration depend on the climatic conditions (T and RH).[16,18] It was concluded that above the thermodynamically predicted deliquescence humidity of phase α, the hydration kinetics is fast as hydration occurs via a solution-mediated mechanism, while below the calculated deliquescence humidity, the hydration proceeds extremely slow as it has to involve a solid-state reaction. The authors further mentioned that hydration via the solid-state reaction is kinetically hindered.

DOI: 10.1021/acs.cgd.8b01908
Cryst. Growth Des. 2019, 19, 2279−2288

Since no direct measurements of the deliquescence pressure are available for the α-phases, these pressures were calculated at room temperature for a "slow hydrating" salt (K_2CO_3) and a "fast hydrating" salt ($MgCl_2{\cdot}4H_2O$). This calculation requires the knowledge of the solubility products of the respective phases and the ability to calculate the activity coefficients and water activities in their saturated solutions. Solubility products can be calculated from the solubility products of the respective β-phases and the equilibrium pressures of their hydration transitions.[39] The ion interaction (Pitzer) model[40] was used to calculate activities. Details of the calculations are provided as Supporting Information S2 and S3. The deliquescence pressures of K_2CO_3 and $MgCl_2{\cdot}4H_2O$ were compared with their critical pressure p^* at which instantaneous hydration occurs. The result is included in the phase diagram in Figure 15.

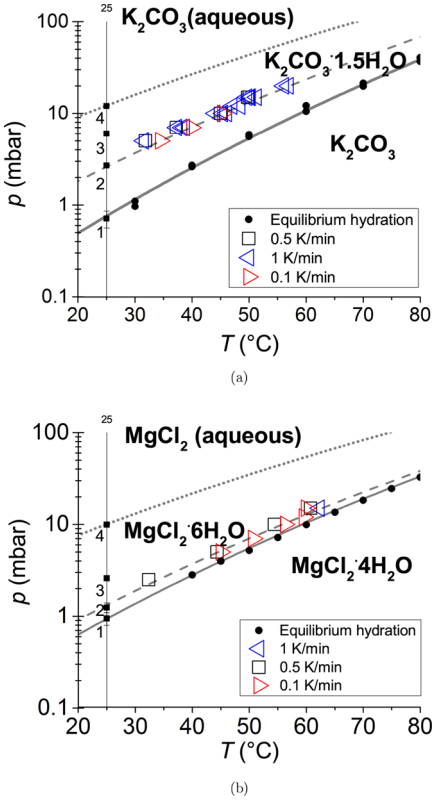

Figure 15. Phase diagrams of K_2CO_3 (a) and $MgCl_2$ (b). At 25 °C the following transitions are indicated: hydration transition at equilibrium (1), instantaneous conversion (i.e., critical pressure p^*) (2), deliquescence of phase α—calculated via the Pitzer equation (3), and deliquescence of phase β (4), adapted from the literature and included for completeness.[29]

Figure 15 shows that for K_2CO_3 and $MgCl_2{\cdot}4H_2O$ the calculated deliquescence pressure (point 3) is roughly 2 times higher than the pressure needed for spontaneous hydration, i.e. hydration without induction time (point 2). Indeed, no macroscopic liquefaction was observed during the hydration experiments. We conclude that the observed metastable zone boundary at $p/p_{eq} \sim 2.5$ for K_2CO_3 is not the pressure for bulk dissolution of the metastable phase since deliquescence is expected at $p/p_{eq} > 8$. However, a wetting layer below the deliquescence point of the metastable phase is expected[41,42] and should be considered when interpreting the induction period and metastable zone.

The wetting layer is expected to be an inherently present layer of water and ions which interacts with the ionic surface at low vapor pressures equivalent to the water monolayer regime, as a result of the strong water-cation interaction.[43] The thickness and mobility of this wetting layer increases with increasing vapor pressure. That is, a correlation between the deliquescence pressure p_d and the wetting layer mobility at $p < p_d$. Around the critical pressure p^* (where noticeable conversion rates start) the surface wetting layer is expected to be thick and any depositing water molecule is expected to lead to conversion. In view of classical nucleation, the wetting layer is a part of the pre-exponential factor κ (i.e., not influencing the energy barrier ΔG^*) in the rate equation.

The small metastable zone in $MgCl_2{\cdot}4H_2O$ is explained by the correlation between the deliquescence pressure p_d and the film mobility at $p < p_d$. The deliquescence at room temperature of $MgCl_2{\cdot}4H_2O$ (2.61 mbar) is at lower water activity compared to K_2CO_3 (6.02 mbar); i.e., the film mobility of $MgCl_2{\cdot}4H_2O$ is high with respect to K_2CO_3 at the equilibrium pressure p_{eq} (point 1), which is roughly the same for $MgCl_2{\cdot}4H_2O$ and K_2CO_3: 0.93 mbar and 0.71, respectively. As a result, the conversion of $MgCl_2{\cdot}4H_2O$ is, for a similar energy barrier ΔG^*, is still higher than the conversion of K_2CO_3 due to the surface mobility.

The generic hydration process is summarized schematically in Figure 16. The interfacial energy γ relates to the mobile salt-solution interface. The interface is expected to be more thick and mobile when the pressure approaches the thermodynamic deliquescence pressure of phase α.

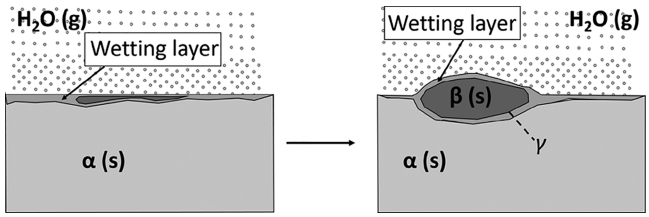

Figure 16. Schematic illustration of the hydration process of a primary crystallite of phase α. The hydration can be regarded as a solid−solid phase transition from phase α to phase β aided by a wetting layer.

Impact on Thermochemical Heat Storage. The atmospheric flow conditions in TGA resemble an open reactor system (open system).[10] As a comparative analysis of thermochemical performance, the lab scale temperature and power output of the four investigated salts are listed. Figure 17 shows the power output as a function of the salt temperature at a working pressure of p = 10 mbar, when the sample is cooled with a rate of 0.1 K/min.

Table 2 is an overview of the temperature and power output of each salt. Although the operation temperature in equilibrium is expected at ca. 60 °C (48 °C for $CuCl_2$), the power−temperature characteristic is different for each salt as a result of the water mobility-related nucleation and growth.

For $CuCl_2$ and K_2CO_3, the metastable zone leads in open reactor conditions to a negligible power output at near-equilibrium pressures and decreases the temperature of maximum power output significantly with respect to the equilibrium temperature; i.e., the output temperature and

DOI: 10.1021/acs.cgd.8b01908
Cryst. Growth Des. 2019, 19, 2279−2288

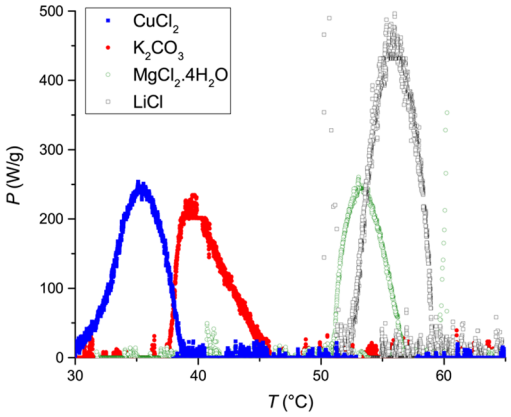

Figure 17. Power output against temperature for the studied thermochemical salts. Hydration was performed at p = 10 mbar with a cooling rate of 0.1 K/min.

Table 2. Overview of the Temperature and Power Output at p = 10 mbar[a]

salt	$T_{equilibrium}$	$T_{onset,TGA}$ °C (±0.5)	$T_{P_{max}}$	P_{max} W/g	MZW K
$CuCl_2$	48	39	35	250	9
K_2CO_3	59	46	40	201	13
$MgCl_2{\cdot}4H_2O$	59	57	53	250	2
LiCl	60	59	56	460	1

[a]The MZW is the difference between the onset temperature in TGA and the equilibrium temperature.

working pressure of a thermochemical salt are limited by its MZW rather than its equilibrium phase diagram.

In order to have a sufficient power output at near-equilibrium temperatures, a crystallite should have nuclei which are able to grow. The crystallite can be triggered by nucleation at e.g. a vapor pressure above the metastable zone, followed by hydration at higher temperature inside the metastable zone (i.e., a prenucleation). Another possibility is to maintain nucleation sites (via operation by partial dehydration or, e.g., the addition of heterogeneous nucleation sites). It should also be noted that growth requires, besides nuclei, the transport of water to the hydrated crystallite; i.e., the surface mobility of water molecules is an important factor for power output besides the nucleus density and deserves further study.

Finally, we note that the MZW depends on reactor aspects such as atmosphere, flow speed, and system size. Therefore, the actual impact of the MZW on reactor performance should be investigated under reactor conditions. Further research should address the MZW in vacuum conditions (closed system).

CONCLUSION

In this work, the hydration of four thermochemical salts ($CuCl_2$, K_2CO_3, $MgCl_2{\cdot}4H_2O$, and LiCl) has been studied. By combining equilibrium and nonequilibrium hydration experiments, phase diagrams as a function of vapor pressure and temperature were obtained and induction time studies as a function of supersaturation could be performed.

On the one hand, it is demonstrated for $CuCl_2$ and K_2CO_3 that the near-equilibrium region involves a metastable zone which can be described by classical homogeneous nucleation theory. On the other hand, it is demonstrated that $MgCl_2{\cdot}4H_2O$ and LiCl hydrate at near equilibrium conditions. It is further shown for K_2CO_3 (metastable) and $MgCl_2{\cdot}4H_2O$ (not metastable) through solubility calculations using the Pitzer ion model that the phase transition is not mediated by bulk dissolution.

It is concluded that the hydration proceeds as a solid−solid phase transition, mobilized by a wetting layer, where the mobility of the wetting layer increases with increasing vapor pressure. At the metastable boundary (where noticeable conversion rates start) instantaneous nucleation is expected.

In view of heat storage application, the finding of metastability in thermochemical salts reveals the impact of nucleation and growth processes on the thermochemical performance. Moreover, it demonstrates that the output temperature and power of a thermochemical salt in atmospheric flow conditions (open system) are limited by its metastable zone width (MZW) rather than its equilibrium phase diagram. Further study should address the MZW in vacuum conditions (closed system). Manipulation of the MZW of salt hydrates by, e.g., prenucleation or heterogeneous nucleation is a potential way to raise the output temperature and power on material level in thermochemical applications.

ASSOCIATED CONTENT

Supporting Information

The Supporting Information is available free of charge on the ACS Publications website at DOI: 10.1021/acs.cgd.8b01908.

Application of the classical nucleation theory to hydration, deliquescence humidities of K_2CO_3 and $MgCl_2{\cdot}4H_2O$, and ion interaction parameters of K_2CO_3 and $MgCl_2{\cdot}4H_2O$ (PDF)

AUTHOR INFORMATION

Corresponding Author

*E-mail: h.p.huinink@tue.nl.

ORCID

Leyla-Cann Sögütoglu: 0000-0002-0412-3468

Notes

The authors declare no competing financial interest.

ACKNOWLEDGMENTS

This project has received funding from the European Unions Horizon 2020 research and innovation programme under grant agreement No 680450. This work reflects only the authors view. The European Commission is not responsible for any use that may be made of this information. The authors thank Hans Dalderop for his technical support.

REFERENCES

(1) Kaygusuz, K. The viability of thermal energy storage. *Energy Sources* **1999**, *21*, 745−755.

(2) Pardo, P.; Deydier, A.; Anxionnaz-Minvielle, Z.; Rougé, S.; Cabassud, M.; Cognet, P. A review on high temperature thermochemical heat energy storage. *Renewable Sustainable Energy Rev.* **2014**, *32*, 591−610.

(3) Solé, A.; Fontanet, X.; Barreneche, C.; Fernández, A. I.; Martorell, I.; Cabeza, L. F. Requirements to consider when choosing a thermochemical material for solar energy storage. *Sol. Energy* **2013**, *97*, 398−404.

(4) Pathak, A. D.; Nedea, S.; Zondag, H.; Rindt, C.; Smeulders, D. A DFT-based comparative equilibrium study of thermal dehydration

DOI: 10.1021/acs.cgd.8b01908
Cryst. Growth Des. 2019, 19, 2279−2288

and hydrolysis of $CaCl_2$ hydrates and $MgCl_2$ hydrates for seasonal heat storage. *Phys. Chem. Chem. Phys.* **2016**, *18*, 10059−10069.
(5) Goldstein, M. Some physical chemical aspects of heat storage. *UN Conf New Sources Energy*, Rome, 1961; pp 411−417.
(6) Bales, C. *Final report of subtask B chemical and sorption storage. Report of IEA Solar Heating and Cooling Programme−Task 32*; 2008.
(7) Aydin, D.; Casey, S. P.; Riffat, S. The latest advancements on thermochemical heat storage systems. *Renewable Sustainable Energy Rev.* **2015**, *41*, 356−367.
(8) Donkers, P. A. J.; Sögütoglu, L. C.; Huinink, H. P.; Fischer, H. R.; Adan, O. C. G. A review of salt hydrates for seasonal heat storage in domestic applications. *Appl. Energy* **2017**, *199*, 45−68.
(9) Lizana, J.; Chacartegui, R.; Barrios-Padura, A.; Valverde, J. M. Advances in thermal energy storage materials and their applications towards zero energy buildings: A critical review. *Appl. Energy* **2017**, *203*, 219−239.
(10) Sögütoglu, L. C.; Donkers, P. A. J.; Fischer, H. R.; Huinink, H. P.; Adan, O. C. G. In-depth investigation of thermochemical performance in a heat battery: Cyclic analysis of K_2CO_3, $MgCl_2$ and Na_2S. *Appl. Energy* **2018**, *215*, 159−173.
(11) Zondag, H.; Kikkert, B.; Smeding, S.; de Boer, R.; Bakker, M. Prototype thermochemical heat storage with open reactor system. *Appl. Energy* **2013**, *109*, 360−365.
(12) Galwey, A. K.; Brown, M. E. *Thermal decomposition of ionic solids: chemical properties and reactivities of ionic crystalline phases*; Elsevier, 1999; Vol. *86*.
(13) Chizhik, S.; Matvienko, A.; Sidelnikov, A. Spatially-ordered Nano-Sized Crystallites formed by Dehydration-Induced Single Crystal Cracking of $CuCl_2{\cdot}2(H_2O)$. *CrystEngComm* **2018**, *20*, 6005−6017.
(14) Zhang, X.; Yin, Q.; Du, W.; Gong, J.; Bao, Y.; Zhang, M.; Hou, B.; Hao, H. Phase transformation between anhydrate and monohydrate of sodium dehydroacetate. *Ind. Eng. Chem. Res.* **2015**, *54*, 3438−3444.
(15) Gonzaga, E. V.; Viana, A. L.; Viana, O. M.; Doriguetto, A. C. Solid-state phase transition mechanism and physical−chemical study of the crystal forms of monosodium alendronate: trihydrate versus anhydrate. *Cryst. Growth Des.* **2016**, *16*, 6891−6902.
(16) Steiger, M.; Linnow, K.; Juling, H.; Gülker, G.; Jarad, A. E.; Brüggerhoff, S.; Kirchner, D. Hydration of $MgSO_4{\cdot}H_2O$ and generation of stress in porous materials. *Cryst. Growth Des.* **2008**, *8*, 336−343.
(17) Aandersson, J. A. N. Y.; de Pablo, J.; Azoulay, M. Kinetics Of the Rehydration of Sodium Sulphide Dehydrated In Situ, Under Formation of Its Pentahydrate. *Thermochim. Acta* **1985**, *91*, 223−234.
(18) Linnow, K.; Niermann, M.; Bonatz, D.; Posern, K.; Steiger, M. Experimental studies of the mechanism and kinetics of hydration reactions. *Energy Procedia* **2014**, *48*, 394−404.
(19) Stanish, M.; Perlmutter, D. Kinetics of hydration-dehydration reactions considered as solid transformations. *AIChE J.* **1984**, *30*, 557−563.
(20) Englert, U.; Ganter, B.; Wagner, T.; Kläui, W. Reversible Topotactic Hydration and Dehydration of an Europium Complex [1]. *Z. Anorg. Allg. Chem.* **1998**, *624*, 970−974.
(21) Mullin, J.; Osman, M. The nucleation and precipitation of nickel ammonium sulphate crystals from aqueous solution. *Krist. Tech.* **1973**, *8*, 471−481.
(22) Volmer, M.; Weber, A. Keimbildung in übersättigten Gebilden. *Z. Phys. Chem.* **1926**, *119*, 277−301.
(23) Mullin, J. W. *Crystallization*; Elsevier, 2001.
(24) Xiao, Y.; Tang, S. K.; Hao, H.; Davey, R. J.; Vetter, T. Quantifying the inherent uncertainty associated with nucleation rates estimated from induction time data measured in small volumes. *Cryst. Growth Des.* **2017**, *17*, 2852−2863.
(25) Jacobsen, J.; Jacobsen, K. W.; Stoltze, P.; Nørskov, J. K. Island Shape-Induced Transition from 2D to 3D Growth for Pt/Pt(111). *Phys. Rev. Lett.* **1995**, *74*, 2295−2298.
(26) Brownstein, S.; Han, N. F.; Gabe, E.; LePage, Y. A redetermination of the crystal structure of cupric chloride dihydrate. *Z. Kristallogr. - Cryst. Mater.* **1989**, *189*, 13−16.
(27) Skakle, J. M.; Wilson, M.; Feldmann, J. Dipotassium carbonate sesquihydrate: rerefinement against new intensity data. *Acta Crystallogr., Sect. E: Struct. Rep. Online* **2001**, *57*, i94−i97.
(28) Jayakumar, A.; Gomez, A.; Mahinpey, N. Post-combustion CO_2 capture using solid:K_2CO_3 Discovering the carbonation reaction mechanism. *Appl. Energy* **2016**, *179*, 531−543.
(29) Greenspan, L. Humidity fixed points of binary saturated aqueous solutions. *J. Res. Natl. Bur. Stand., Sect. A* **1977**, *81*, 89−96.
(30) Gabbott, P. *Principles and applications of thermal analysis*; John Wiley & Sons, 2008.
(31) Glasser, L. Thermodynamics of inorganic hydration and of humidity control, with an extensive database of salt hydrate pairs. *J. Chem. Eng. Data* **2014**, *59*, 526−530.
(32) Polyachenok, O.; Dudkina, E.; Polyachenok, L. Thermal stability and thermodynamics of copper(II) chloride dihydrate. *J. Chem. Thermodyn.* **2009**, *41*, 74−79.
(33) Carling, R. Dissociation pressures enthalpies of reaction in $MgCl{\cdot}2H_2O$ and $Cacl_2{\cdot}nNH_3$. *J. Chem. Thermodyn.* **1981**, *13*, 503−512.
(34) Washburn, E. *International Critical Tables of Numerical Data, Physics, Chemistry and Technology*, 1st electronic ed.; Knovel, 2003.
(35) Chen, R.; Kirsh, Y. *The analysis of thermally stimulated processes*; Elsevier, 2013.
(36) Felbinger, A.; Neels, H. Die Natriumbikarbonat-Kristallisation im Ammoniak-Soda-Prozeß. *Krist. Tech.* **1966**, *1*, 137−146.
(37) Nielsen, A. E.; Söhnel, O. Interfacial tensions electrolyte crystal-aqueous solution, from nucleation data. *J. Cryst. Growth* **1971**, *11*, 233−242.
(38) Machlin, E. *An introduction to aspects of thermodynamics and kinetics relevant to materials science*; Elsevier, 2010; pp 134−143.
(39) Steiger, M. Thermodynamic properties of $SrCl_2$ (aq) from 252 to 524 K and phase equilibria in the − $SrCl_2$−H_2O system: Implications for thermochemical heat storage. *J. Chem. Thermodyn.* **2018**, *120*, 106−115.
(40) Pitzer, K. S. *Activity coefficients in electrolyte solutions*; CRC Press: Boca Raton, FL, 1991; pp 75−153.
(41) Gough, R.; Chevrier, V.; Baustian, K.; Wise, M.; Tolbert, M. Laboratory studies of perchlorate phase transitions: Support for metastable aqueous perchlorate solutions on Mars. *Earth Planet. Sci. Lett.* **2011**, *312*, 371−377.
(42) Andersson, J.; Azoulay, M.; de Pablo, J. Kinetic investigation of the sorption of water by barium chloride monohydrate. *Thermochim. Acta* **1983**, *70*, 291−302.
(43) Cabrera-Sanfelix, P.; Sanchez Portal, D.; Verdaguer, A.; Darling, G. R.; Salmeron, M.; Arnau, A. Spontaneous emergence of Cl-anions from NaCl (100) at low relative humidity. *J. Phys. Chem. C* **2007**, *111*, 8000−8004.

DOI: 10.1021/acs.cgd.8b01908
Cryst. Growth Des. 2019, 19, 2279−2288